Journal of Structural Geology 32 (2010) 1375–1391

Contents lists available at ScienceDirect

Journal of Structural Geology

journal homepage: www.elsevier.com/locate/jsg

Evolution of fault zones in carbonates with mechanical stratigraphy – Insights from scale models using layered cohesive powder

Heijn W. van Gent [a,*], Marc Holland [a,1], Janos L. Urai [a], Ramon Loosveld [b]

[a] Structural Geology, Tectonics and Geomechanics, RWTH Aachen University, Lochnerstraße 4-20, D-52056 Aachen, Germany
[b] Shell Exploration & Production Company, 200 N. Dairy Ashford, Houston, TX 77079, USA

ARTICLE INFO

Article history:
Received 18 January 2008
Received in revised form
30 April 2009
Accepted 4 May 2009
Available online 19 May 2009

Keywords:
Analogue modelling
Dilatant faults
PIV
Hemihydrate
Graben
Carbonate
Caves
Cam-Clay
Fault zone

ABSTRACT

We present analogue models of the formation of dilatant normal faults and fractures in carbonate fault zones, using cohesive hemihydrate powder ($CaSO_4 \cdot ½H_2O$). The evolution of these dilatant fault zones involves a range of processes such as fragmentation, gravity-driven breccia transport and the formation of dilatant jogs.

To allow scaling to natural prototypes, extensive material characterisation was done. This showed that tensile strength and cohesion depend on the state of compaction, whereas the friction angle remains approximately constant. In our models, tensile strength of the hemihydrate increases with depth from 9 to 50 Pa, while cohesion increases from 40 to 250 Pa. We studied homogeneous and layered material sequences, using sand as a relatively weak layer and hemihydrate/graphite mixtures as a slightly stronger layer.

Deformation was analyzed by time-lapse photography and Particle Image Velocimetry (PIV) to calculate the evolution of the displacement field. With PIV the initial, predominantly elastic deformation and progressive localization of deformation are observed in detail. We observed near-vertical opening-mode fractures near the surface. With increasing depth, dilational shear faults were dominant, with releasing jogs forming at fault-dip variations. A transition to non-dilatant shear faults was observed near the bottom of the model. In models with mechanical stratigraphy, fault zones are more complex. The inferred stress states and strengths in different parts of the model agree with the observed transitions in the mode of deformation.

1. Introduction

Carbonate reservoirs contain a large part of the world's hydrocarbon supply (Arnott and Van Wunnik, 1996; Otrtuno-Arzate et al., 2003; Borkhataria et al., 2005; Ehrenberg and Nadeau, 2005). Many carbonates at shallow depth are strong relative to the mean effective stress; because their cohesion and high tensile strength allow them to sustain open fractures and cavities over many scales. These dilational structures focus the flow of fluids, influencing the hydraulic behaviour considerably (Arnott and Van Wunnik, 1996; Sibson, 1996; Billi et al., 2003; Ferrill and Morris, 2003; Otrtuno-Arzate et al., 2003; Billi and Storti, 2004; Crider and Peacock, 2004; Holland et al., 2006; Galland et al., 2006; Bussolotto et al., 2007; Breesch et al., 2009). This increase of structural permeability (Sibson, 1996) with deformation is important for hydrocarbon production (Arnott and Van Wunnik, 1996; Sapra, 1997; Van Konijnenburg et al., 2000; Kerans, 2002; Ehrenberg and Nadeau, 2005; Casabianca et al., 2007). Dilatant faulting could also help to explain the formation of some fault caves that have formed in association with tectonic faults and are not solely the result of dissolution (e.g. Gilli et al., 1999; Margielewski and Urban, 2003).

One cause for the formation of open segments along a fault is the change of the dip angle of shear fractures, which is quite common in mechanically stratified sequences (Wallace, 1861; Dunham, 1948, 1988; Ramsay and Huber, 1987; Peacock and Zhang, 1993; Sibson, 1996, 2000; Mandl, 2000; Ferrill and Morris, 2003; Schöpfer et al., 2007a). Ferrill and Morris (2003) described kite-shaped dilational jogs along fault traces in bedded carbonates in the Cretaceous Buda Limestone (western Texas, USA), deformed at a depth of less than 1 km. The faults show a systematic increase of the dip angle in the more competent layers of the succession, and steeper fault segments dilate to form open jogs. The cavities presently contain a calcite vein fill, resulting from increased vertical infiltration and along-strike fluid flow.

* Corresponding author. Tel.: +49 241 80 95416; fax: +49 241 80 92358.
E-mail address: h.vangent@ged.rwth-aachen.de (H.W. van Gent).
[1] Present address: GeoMechanics International, Emmerich-Josef Straße 5, 55116 Mainz, Germany.

0191-8141/$ – see front matter © 2009 Elsevier Ltd. All rights reserved.
doi:10.1016/j.jsg.2009.05.006

Another cause for open fractures is Mode I tensile fracturing near the surface. In the basalts of north-eastern Iceland, tensile deformation structures dominate in the upper hundreds of meters, which grade through hybrid mode structures to pure shear faults at depths of roughly 1 km (Angelier et al., 1997).

Good quality outcrops of massively dilatant fault zones in carbonates are rare. Outcrops in Tertiary carbonates on Jebel Hafeet, on the border between the United Arab Emirates and Oman, expose some examples in carbonates deformed at shallow depths. Jebel Hafeet is one of a series of foreland anticlines of the Oman Mountains (Noweir, 2000). The young back-thrust-related anticline shows abundant normal fault systems parallel to the fold axis, which are interpreted to be related to outer-arc extension and uplift (Fig. 1). These normal fault zones in the area can be massively dilatant. Apertures of several decimetres are common, predominantly filled with carbonate veins, crushed wall rock or sediments (Fig. 1a and b). These sediments differ from the wall rock and often show a clear stratification. This suggests episodic sedimentation within the fault zones by either gravitational or hydraulic transport. Wide surface fissures are common on the mountain crest. These open structures strike parallel to the fold axis of the anticline (Fig. 1c and d), have opening magnitudes of more than a meter, and show angular blocks of carbonate, dislodged and rotated between the parallel walls (Fig. 1c), but their depth is difficult to access due to both the material infill and the outcrop conditions. The dilatant structures of the fault zones must have a strong effect on hydraulic circulation, suggesting that the caves of the Jebel Hafeet region are fault-related.

The present study is a follow-up of the experiments of Holland et al. (2006) with hemihydrate powder ($CaSO_4 \cdot ½H_2O$) to study the deformation of layered cohesive rocks in the upper crust through a series of scaled analogue models of a buried graben system in carbonates. In the first section of this paper, experiments to measure the material's characteristics are presented. The second section presents the results of a series of scaled analogue models of normal faults in hemihydrate powder, focussing on the effects of mechanical stratigraphy.

Physical modelling has a long history in geosciences (e.g. Cloos, 1930; Hubbert, 1937). Depending on the tectonic and structural processes modelled, a large variety of materials have been used; the most common is sand (Buiter et al., 2006; Schreurs et al., 2006). Recent studies on sand have shown complex strain-hardening behaviour prior to Mohr–Coulomb failure and asymptotic strain-softening (Schellart, 2000; Lohrmann et al., 2003; Panien, 2004; Schreurs et al., 2006). Dry sand does not have a tensile strength, only a small apparent cohesion and is unable to sustain open fractures (Schellart, 2000; Holland et al., 2006). The large grain size of sand produces relatively wide shear zones, as opposed to discrete failure planes (Horsfield, 1977; Lohrmann et al., 2003).

Much less attention has been given to model materials with tensile strength. Wet clay has been used as a material for brittle deformation, but the presence of open fractures was not analyzed in detail (Cloos, 1930; An, 1998). Cohesive materials were used to model volcano-tectonic processes and pit chain formations on Mars (Cailleau et al., 2003; Sims et al., 2003). Other materials include sand made cohesive by capillary forces (Cardozo et al., 2002), cement mixtures for the modelling of coal mine collapse (Xiao, 1993), fine grained silica powder (Galland et al., 2006) and dry hemihydrate powder (Holland et al., 2006). However, the

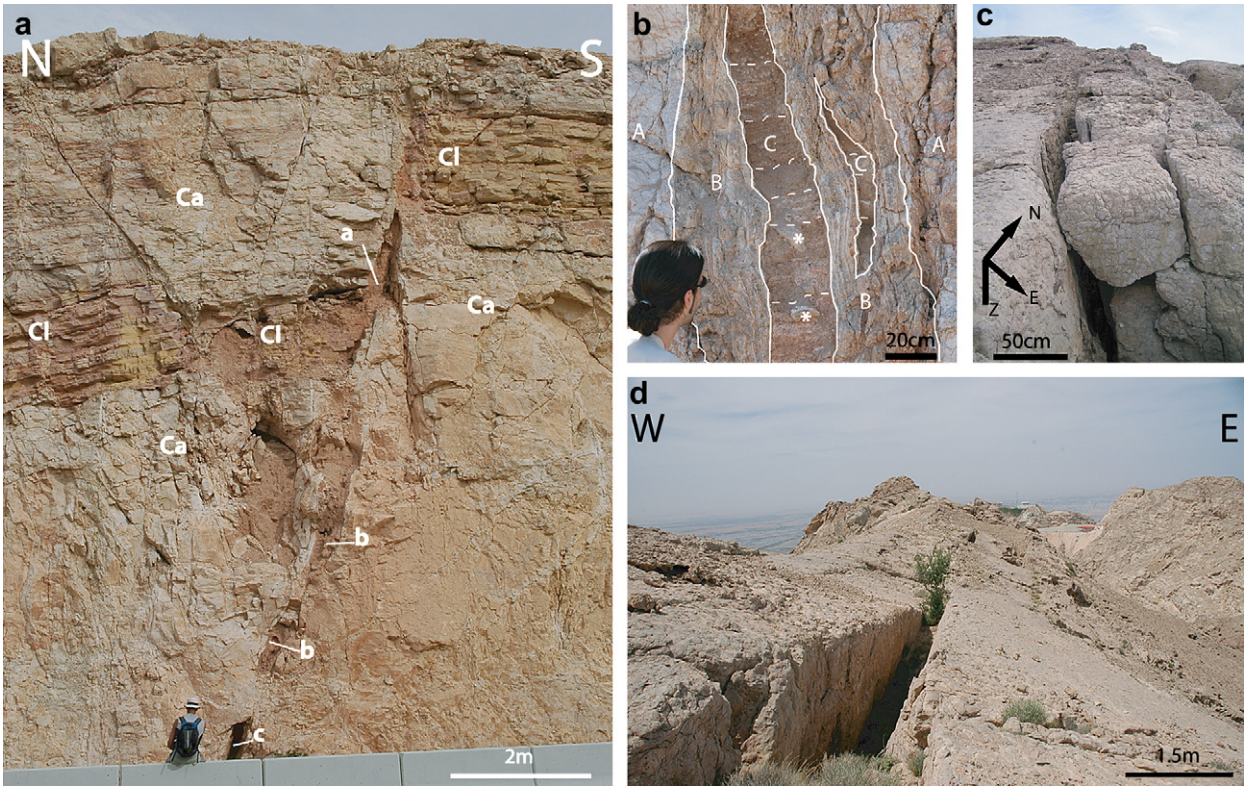

Fig. 1. (a) Normal fault zone in a competent carbonate (Ca), with approximately 3 m offset, showing strongly variable internal structure, width of the fault cavities and clastic infill. Material from a mechanically weaker, slightly more clayey carbonate layer (Cl) is included in the fault zone both between the up- and downthrown parts of the clastic deposits (a), as well as in cavities further down-dip (b). Also note the empty cavity in the bottom of the picture (c). (b) Opening-mode fracture showing layered clastic infill. On the wall rock (A) a rim of precipitated calcite (B) covers the fracture walls. The centre of the fracture (C) is filled with stratified unconsolidated sediments. Stars indicate decimetre size clasts. (c, d) Tensile open mode fissures parallel to the fold crest of Jebel Hafeet. Within the massive fissures blocks of wall rock are rotated (all images taken at Jebel Hafeet, U.A.E.).

mechanical properties of these model materials (e.g. tensile strength), were not well characterised.

In the analogue models described here, the pore fluid is air. As Sibson (1996) pointed out, the formation of structurally permeable mesh structures is primarily fluid-driven in regions of high overpressure, but as long as the cohesion is much higher than the mean stress, fault-fracture meshes can form without overpressures. A process that we are unable to model, but which is extremely important in natural carbonates is pressure solution. Many authors (e.g. Peacock and Sanderson, 1995; Sibson, 1996; Willemse et al., 1997; Micarelli et al., 2005; Agosta and Aydin, 2006; Tondi, 2007) discuss the importance of pressure solution and mineral deposition on the fault initiation and evolution and on permeability anisotropy in natural carbonates.

2. Material properties

2.1. Material properties of hemihydrate powder

The hemihydrate powder ($CaSO_4 \cdot ½H_2O$) used is a commercially available product ("Schnell Gips" from Knauf). Crystals form irregular clusters with sizes between 10 and 400 μm. The grain density of hemihydrate is 2730 kg/m^3 (Gipsindustrie, 2003). The density of dry hemihydrate powder is ~732 kg/m^3, with a porosity of 75%. In order to enhance the images for Particle Image Velocimetry (PIV) analysis (see Section 5); 2.5% of blue marker sand was mixed into the hemihydrate.

2.1.1. Material properties related to preparation

Hemihydrate powder is sensitive to small mechanical perturbations; therefore the effects of sample preparation were studied as a function of both air humidity and differences in sieving.

The moisture uptake of hemihydrate powder under a constant air humidity of 75.2% (inside a container with saturated NaCl-solution at 23 °C, Lide, 1995) is approximately 2–2.5 wt.-% over 2.5 days. Air humidity in the sand box laboratory was between 50 and 60% and the hemihydrate powder was stored there for at least 3 days before the experiments were carried out to limit the variations in moisture content between experiments.

Measuring densities of powder sieved from different sieve heights (SH) showed that the bulk density of the powder increases linearly with SH (Fig. 2) up to 30 cm. Falling from heights >30 cm, the grains reach a terminal velocity and density does not increase, but shows a relatively large variability. This could result from air flow in the laboratory.

2.1.2. Compaction

Compaction measurements under progressively increasing overburden were performed optically between 100 and 1500 Pa by a PIV analysis (see below) and by using an odometer between 0.1 and 300 kPa. In the PIV analysis a 4 cm column of hemihydrate powder was loaded by sieving sand into a cylindrical glass container. Digital photos of this process were analyzed with PIV to derive the vertical strain as a function of depth. This was then converted to change in void ratio, Δe, where:

$$e = \Phi/100 - \Phi$$

Here, Φ is the porosity (Lambe and Whitman, 1969; Muir Wood, 1990).

The results of the two experiments are shown together in Fig. 3. Two clear deviations from the overall trend are visible. At high stresses, the reduced compaction coefficient is reduced. This is interpreted to result from the collapse of the hemihydrate clusters, while at very low stresses the reduced compaction is interpreted to result from elastic deformation (Lambe and Whitman, 1969; Muir Wood, 1990). This "pseudo-burial"-related initial strength is interpreted to be due to compaction resistant electrostatic forces, providing a minimum void ratio of the powder. The transition to normal compaction occurs at about 650 Pa, corresponding to a burial of about 9.5 cm in a hemihydrate pile.

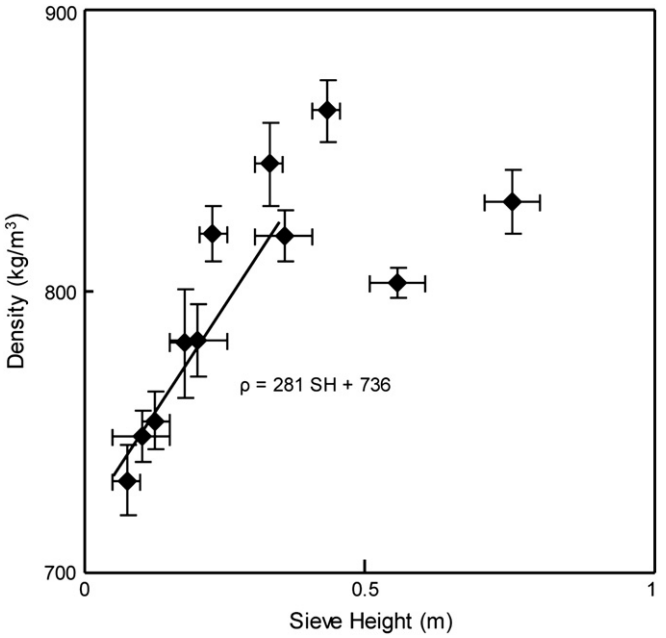

Fig. 2. Evolution of mean density of sieved hemihydrate powder, as a function of sieve height. Vertical error bars represent standard deviation in density, horizontal error bars are used to indicate the spread in falling distance. The line is the linear trend line for data with SH < 0.3 m.

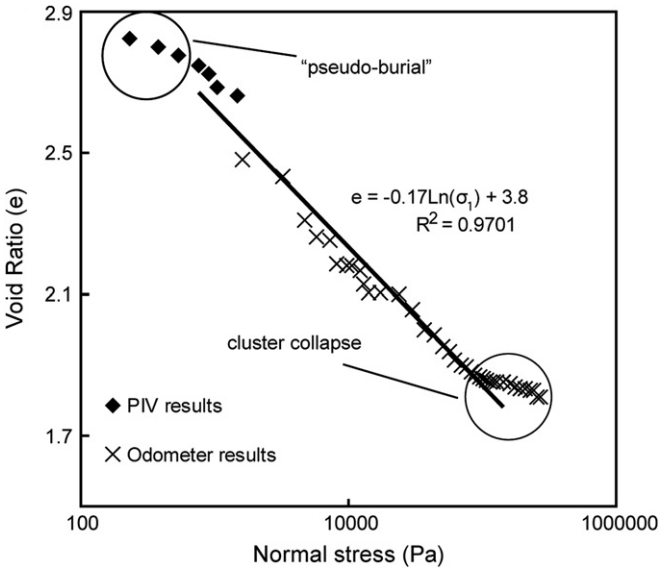

Fig. 3. Combined results of compaction experiments for hemihydrate, using an odometer and PIV analysis. The trend line in this figure is constructed using data of 650 Pa < stress < 70,000 Pa. At low stress values the void ratio values are lower than the trend line. This is the result of the "pseudo-burial" effect, an initial strength which needs to be overcome before compaction starts. At high loads the collapse of the clusters also results in a deviation from the trend.

2.1.3. Shear tests

Mohr–Coulomb failure envelopes of hemihydrate powder were determined with a modified Jenike shear cell (Van der Zee, 2001). We performed 'overconsolidated' and 'normally consolidated' shear tests (Figs. 4 and 5). A normally consolidated shear test is a standard shear test, where the shear strain/shear stress plateau value is used as the failure locus (see Fig. 4a).

'Overconsolidation' involves pre-compaction of the sample. The vertical loading of the sample in the shear cell is followed by horizontal shearing to establish the normally consolidated failure locus. Then, the horizontal shear force is removed and the vertical load is reduced. In the following step, the horizontal load is reapplied and an overconsolidated shear locus is measured (see Fig. 4b; see also Schweiger and Zimmermann, 1999; Holland et al., 2006). By further stepwise reduction of the vertical stress, multiple overconsolidated shear tests can be performed on a single sample. These experiments are essential to correctly interpret normal faulting experiments, because of the progressive reduction in mean effective stress. The failure envelopes of both types of test are shown in Fig. 5.

The initial void ratio was calculated for each overconsolidated shear test (see inset of Fig. 5a and b). The coefficient of internal friction is roughly constant for all tests (~0.6), but the cohesion increases linearly with increasing pre-compaction (Fig. 5b). The measured cohesion of uncompacted hemihydrate is ~40 Pa. During shear tests, a vertical LVDT (Linear Variable Differential Transformer) showed a compaction of about 10%.

Holland et al. (2006) used a slightly different hemihydrate product. They also used the overcompacted shear tests in their material characterisation, but did not separate the results by initial void ratio. As a result, their best fit failure envelope is curved, but the curve agrees well with the failure envelopes of this study (Fig. 5c). Analyses of stress/strain curves in multiple shear experiments suggest the onset of plasticity is at approximately 0.2% strain.

2.1.4. Tensile strength

A simple way to estimate tensile strength is to measure the maximum height of an unsupported powder column, by pulling apart two juxtaposed sheets of paper, on which a layer of powder is sieved. The maximum height of a free-standing wall is 7 cm for our material.

As for cohesion (Fig. 5b), the effect of pre-compaction on tensile strength was measured by using a device that measures a powders' tensile strength at the University of Würzburg (Schweiger and Zimmermann, 1999). The standard pre-compaction is at 130 Pa, but manual control of the device allowed measurement of the tensile strength at pre-compaction stresses between 60 and 440 Pa (Fig. 6). This pre-compaction stress was converted to void ratio. The tensile strength of uncompacted powder is 9 Pa, with a linear increase of tensile strength with progressive compaction (Fig. 6).

2.1.5. Constitutive model

Our experiments show that both cohesion and tensile strength of hemihydrate powder are a function of (initial) compaction, while the coefficient of internal friction remains roughly constant. This influences the way faults and fractures form, since the fault-dip angles in frictional materials depend on the tensile strength and friction angle of the material (Hancock, 1985; Parry, 1995; Ferrill and Morris, 2003).

To describe dilatant behaviour in soils as a function of pore volume, the Cam-Clay model was developed by Roscoe and Schofield (1963). In Fig. 7 the shear test, compaction and tensile strength results are combined in a 'Cam-Clay' type of plot. The initial void ratio is plotted along one axis, and the other two axes represent the normal stress and shear stress. Obviously, the data available do not allow construction of an accurately constrained Cam-Clay model. For example, during shear tests, the vertical LVDT recorded volume changes up to 10%. In Fig. 7 we thus plotted the initial void ratio rather than the actual void ratio at failure. The "pseudo-burial" effect is also presented in the model. Fig. 7 is a useful summary of material properties, and is sufficient for scaling our models. For the definition of the full Cam-Clay constitutive model (Jones and Addis, 1986; Jones et al., 1991; Callari et al., 1998), e.g. for accurate geomechanical modelling of our experiments, more work is needed.

2.2. Material characterisation of the sand

Sand was used to create a mechanical stratigraphy in some experiments. The sand (0.1–0.4 mm) has a density of 1354 kg/m^3 with a porosity of 50.8%. The coefficient of internal friction is 0.53

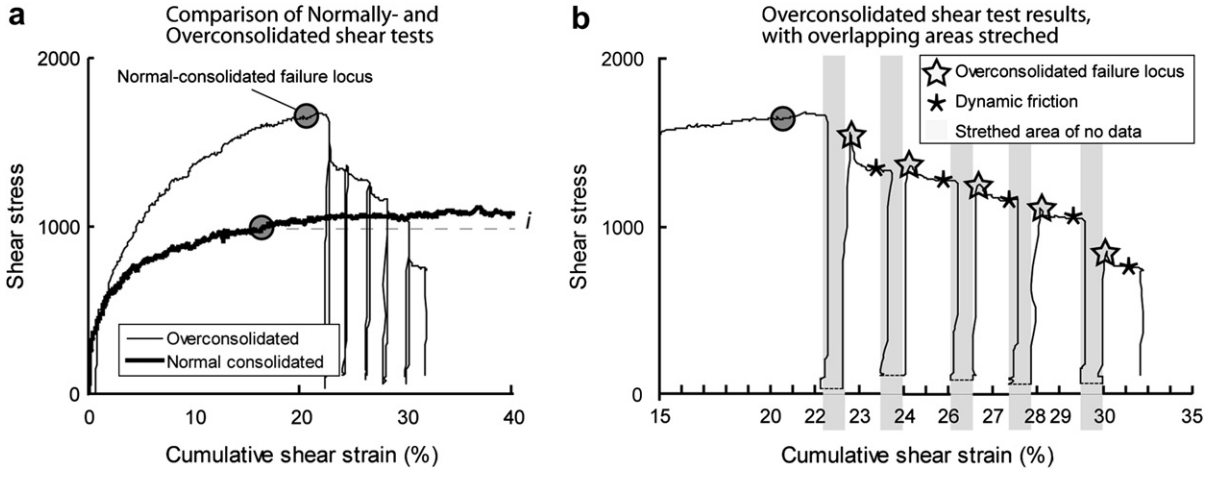

Fig. 4. (a) Typical examples of stress/strain relations in normally and overconsolidated shear tests. In the normally consolidated shear test, the vertical stress was 1374 Pa, in the overconsolidated shear test, the initial vertical stress was 2520 Pa. Indicated are the normally consolidated failure loci for both tests. With increasing shear strain, the shear stress continues to increase slowly (distance *i*), as a result of sample surface reduction due to fragmentation. (b) A detailed view of part of the overconsolidated shear test. To show the peak stress during each cycle of loading, the corresponding parts of the graphs were displaced, with the gap indicated by a grey zone. The peak stress corresponds to the critical shear stress at brittle failure, while the dynamic shear stress is the result of the friction on the fracture itself. In five steps, this initial vertical stress was reduced, resulting in five peak shear stress and dynamic shear stress data points.

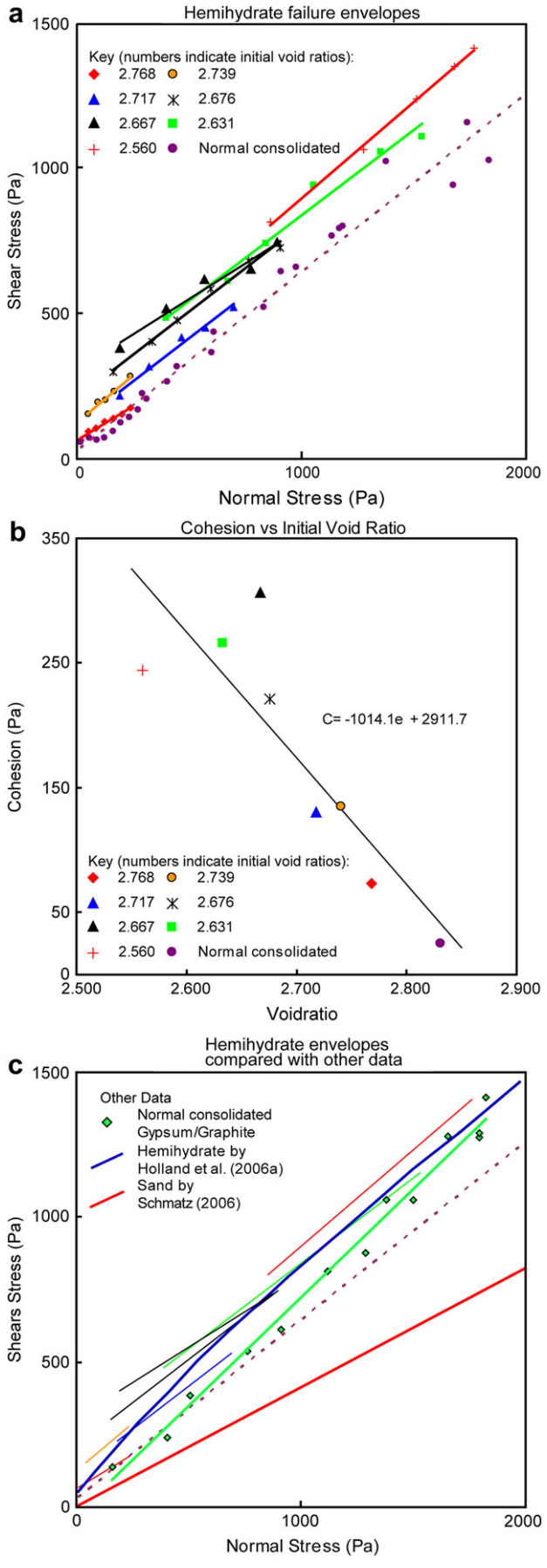

(Schmatz, 2006). Since dry sand has no true cohesion (Schellart, 2000), it is weaker at a low normal stress than hemihydrate powder. The failure envelope of the sand is shown in Fig. 5c.

2.3. Material characterisation of the hemihydrate/graphite mixtures

In one experiment mechanical layering was introduced using layers of a mixture of hemihydrate and graphite powder at a ratio of 2–1. The coefficient of internal friction is 0.75, and under the conditions of our experiments the normally compacted powder is slightly stronger than the hemihydrate powder (see also Fig. 5c).

3. Scaling

Our model can be scaled to natural prototypes using scaling laws of Hubbert (1937) and Ramberg (1981). The effect of a scale reduction on any material quantity can be defined by a ratio of this quantity (Θ) between the model (Q_m) and the prototype (Q_p) (Hubbert, 1937; Ramberg, 1981).

The material properties of carbonates in the upper crust vary greatly. Table 1 shows a collection of material properties of natural carbonates from literature. Using the properties of the porous limestone from the Southern Netherlands (see Table 1, Bekendam, 1998), we obtain a scaling ratio of 1 to 8.1×10^3–9.7×10^3, or 1 cm of the experiment equals 81–97 m of prototype.

Large rock bodies are significantly weaker than small rock samples (Griffith, 1921; Hoek, 2007). In this case 1 cm in our model would correspond to 8–10 m of calcarenite. More data on the sample size and the effect on material strength are required to calculate a more precise scaling ratio.

To check the scaling of our model material with the prototype over the whole depth range is much more difficult. Our experiments represent a sediment pile that is normally consolidated at the surface, which progressively compacts and becomes more cohesive with burial.

4. Methods and experimental setup

The setup used in this work is an adaptation of the deformation box used by Holland et al. (2006) (Fig. 8). It consists of a 70 × 15 cm wide deformation rig, tightly fitted between two low-friction glass plates. The maximum horizontal elongation is 11%.

The master faults of the deformation rig dip 60°. The graben block is pulled down using an electric motor (vertical displacement rate: 0.0166 mm/s). This forces the horst blocks to slide outward, creating a master graben structure.

To fill the box with a constant sieve height and thus with constant layer density, a table with a pre-tensioned steel mesh (1 mm mesh size) was constructed. This table stands 30 cm above the box. The box is filled by scraping the top of this mesh covered by hemihydrate with a scraper. The same method was used to prepare

Fig. 5. (a) Mohr space representation for the failure loci of hemihydrate, for normally and overconsolidated shear tests. The data for the overconsolidated shear tests have been grouped per individual shear test and thus have a common initial pre-compaction. This pre-compaction has been used to calculate a void ratio which is shown in the key. (b) The calculated cohesion for every overconsolidated shear test as a function of the initial void ratio. Every data point represents the intersection of the trend lines shown in (a) with the shear stress axis. Here C is the cohesion in Pa, and e is the initial void ratio. (c) The hemihydrate failure envelopes of 5(a) compared with the different materials in this study. Shown are the hemihydrate characterisation of Holland et al. (2006), the characterisation of the sand by Schmatz (2006), and the normally consolidated shear test measurements and the trend line of the hemihydrate/graphite mixture.

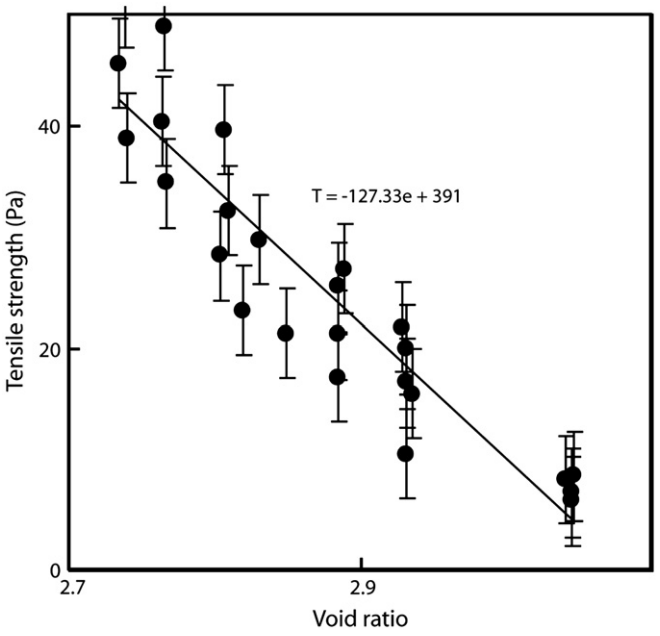

Fig. 6. The tensile strength measurements as a function of void ratio. The solid line represents trend line. *T* is the tensile strength (Pa) and *e* is the void ratio. A standard deviation of ±10 Pa in the data is within the normal scatter of the analysis (S. Dünisch, personal communication, 2005).

the graphite/hemihydrate layers. The sand layers were made using a funnel shaped cart that runs on tracks on the sieve table.

The experiments were recorded using two digital cameras, for overview and detailed observations. Both cameras were computer controlled and recorded high resolution (3000 × 2000 pixel, raw format) images every 30 s.

Leaving the experiment overnight after preparation increases the strength of the model in such a way that notable differences were observed in comparison with experiments that were deformed directly after preparation (Holland et al., 2006). To avoid this effect we set up and ran the experiments within 3 h.

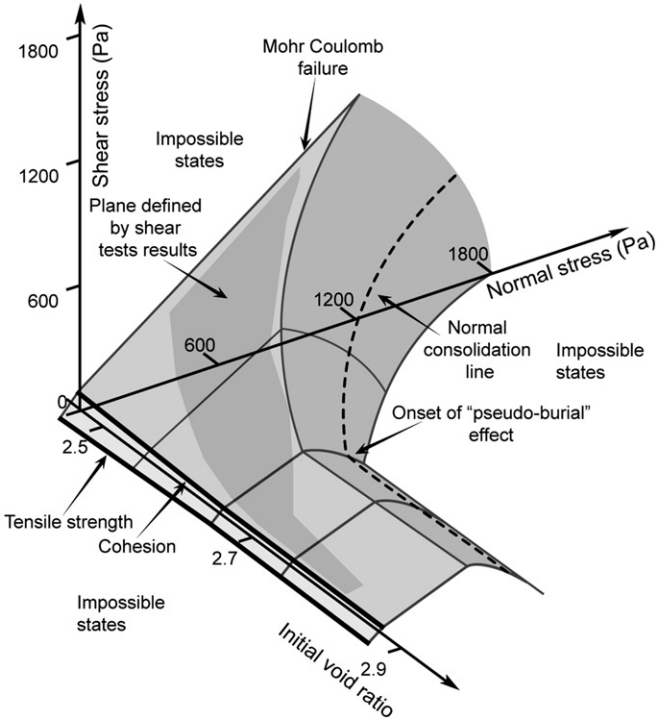

Fig. 7. Combination and interpretation of all material characterisation data, plotted in a 'Cam-Clay-type' of plot. Note that along the *x*-axis the normal stress is plotted, along the *y*-axis the shear stress, and along the *z*-axis the initial void ratios are plotted. Bold black lines represent measured data; the dark plane on the Mohr–Coulomb failure plane represents data from the shear tests. Also the effect of "pseudo-burial" is presented.

5. PIV

To analyze the experiments, PIV analyses were done on the digital images. PIV is a non-intrusive, optical technique to observe movements and flows. Originally developed for gas and fluid flows (Baldassarre et al., 2001), it has recently been applied to geological analogue models (e.g. Wolf et al., 2003; Adam et al., 2005; Holland et al., 2006; Schmatz, 2006; Schmatz et al., in press).

The resolution of the displacement in these analyses is 0.5 pixel. This means that the early stages of the evolution of structures can be detected. The PIV-software package used in this research is DaVis from LaVision.

6. Experiments

The series of experiments was designed to investigate the influence of mechanical stratigraphy on the development and geometry of the evolving structures. Six different experiments were performed, one using pure hemihydrate, four experiments with different geometries of intercalated sand layers, and one with four intercalated hemihydrate/graphite layers (Fig. 9). Although obvious differences are present between individual experiments, the large-scale geometry of the structures is generally similar, forming a symmetric graben with a pronounced surface expression. Control experiments with the same initial geometry show that the experiments are reasonably reproducible, but not in the finer details of the fracture system. Observations of the shape of the fractures both in side- and top view, as well as in horizontal sections suggest that they are not strongly influenced by the interaction with the glass side plates.

Fig. 9 shows an image of the final stages of all experiments. All experiments show a graben with a pronounced surface expression and vertically walled cliffs and Mode I fractures at the surface. At mid-depths in the box the shear faults show open dilational jogs (examples are present in all experiments, but are best expressed in Fig. 9f), while at the base of the box non-dilatant shear faults formed.

6.1. Initial deformation in pure hemihydrate and experiments with graphite layers

Initial deformation in the models is best observed in the PIV output because the evolving discontinuities are present in the models before they can be detected visually. High resolution analyses of the early stages of these experiments are essential, especially because velocity fields can be quantitatively compared with numerical simulations (Buiter et al., 2006; Schreurs et al., 2006).

Fig. 10 shows several frames from experiment 6, overlain by the incremental displacement vector field, calculated with PIV. This experiment contains four layers of the slightly stronger graphite/hemihydrate mixture. After 0.3% of the total 11% elongation (Fig. 10a), the displacement field is continuous. The downward movement of the hangingwall and the fixed footwall results in a high displacement gradient around the top of the basement fault. An approximately 15 cm wide transition zone occurs close to the surface. No brittle structures are observed at this step.

After an elongation of 0.6%, a Mode I fracture propagates downwards from the surface (Fig. 10b). The displacement field

Table 1
Summary of carbonate and marble material properties. ρ is density, μ is the coefficient of internal friction, C is cohesion and E is Young's Modulus.

Rock type, location	ρ (kg/m^3)	μ	C (MPa)	E (MPa)	Reference
Maastricht Fm calcarenites, SE Netherlands	1274–1530	0.31	0.68	300–1000	Bekendam (1998)
Redwall limestone, Arizona	2640	0.7–1.7	13–36	55	Birch (1966)
Solenhofen limestone, Germany	2480–2712	0.53	105	57–63	Birch (1966), Turcotte and Schubert (2002)
Leuders limestone, Texas	–	0.53	15	–	Turcotte and Schubert (2002)
Limestone, general	1600–2700	–	–	10–70	Schellart (2000)
Marble, general	2670–2750	0.75	110	23–28	Schellart (2000), Turcotte and Schubert (2002)

shows a clear discontinuity across the fracture, while deeper in the model the displacement field is still continuous.

After an elongation of 1.5%, an almost vertical, upward propagating set of en-echelon fractures develops (Fig. 10c). A Mode I fracture forms at the surface between this set and the first fracture. The fracture initiated in Fig. 10b propagates downward and displays a clear break in dip angle at the transition between the Mode I opening and extensional shear faulting (top intercalated layer). The displacement field shows that the bulk of the extension is taken up at the vertical fracture set, while the short arrows between this set and the first Mode I fracture indicate that this block slides only a small distance along the extensional shear fault. This jump in localized deformation is accompanied by a bedding-parallel shear in a graphite/hemihydrate layer, shown by a 30° clockwise rotation in the velocity field in the second intercalated layer from the bottom. Here the blue vector colour indicates a decrease in displacement magnitude. The swirling arrows at the surface indicate rotation.

After an elongation of 2.0% (Fig. 10d) a new fracture develops through the block between the vertical fracture set and the first Mode I fracture. The displacement field shows that the two blocks closest to the centre of the box are still actively moving while the other blocks remain stationary. At an elongation of 3.1%, the fault which formed last becomes the main structure and will remain dominant until the end of the experiment (Fig. 10e). The displacement field shows no slip on any of the older structures.

6.2. Initial deformation in experiments with sand layers

In experiments with sand layers, the initial faults are more segmented than those in the models with only hemihydrate and hemihydrate/graphite mixture. After 0.6% of bulk extension (Fig. 11a1), an array of sub vertical fractures formed (Schöpfer, et. al., 2007c), across the sand layers which do not fully cross the hemihydrate. After an elongation of 0.8% (Fig. 11a2), these fractures evolved into the segments of an incipient fault zone with a much higher dip angle than the basement fault. During further deformation this leads to the initiation of new fractures in the footwall (Fig. 11a3). In Fig. 11b a succession of images shows the development of a downward propagating fracture, segmented when it passes layer boundaries. Note that this fracture is initiated at the same amount of elongation as the segmented fault in Fig. 11a, but it forms at a larger distance from the master fault (see Fig. 9e), suggesting decoupling by the sand layers. The fracture shows an increase of dip as it approaches the second sand layer from the top. After an elongation of 0.8%, this fracture stops developing, due to the development of a vertical fracture in the footwall.

When the fracture in Fig. 11c cuts through the sand layers, it becomes steeper. This fracture formed in the upper left of Fig. 11b3, and takes over strain from the fault in Fig. 11b. The development of an en-echelon set of fractures (Fig. 11c) is very similar to the one in Fig. 11a.

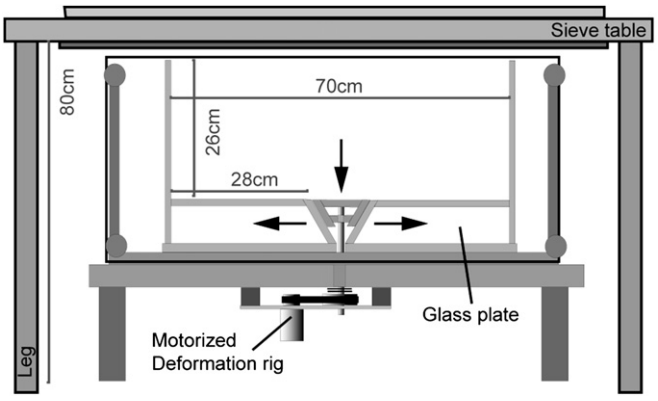

Fig. 8. The deformation table in profile view. Note the sieve table, which ensures a constant sieve height. Also shown are the motorized deformation rig and the moving tables.

6.3. Later structures and overview of structural evolution

In this section a general description of the most important structures observed in the later experimental stages is given, using the final geometry of experiment 6 as an example (Fig. 12). This experiment was chosen because it contains most of the structures observed throughout the series of experiments. Images of the early evolution in parts of this experiment are shown in Fig. 10 and later deformation is shown in Fig. 13.

Vertical Mode I fractures (key 1 in Fig. 12) at the surface generally are the first structures to form (Figs. 10b and 11). Typically one to three of these cracks form on the surface, on both sides of the centre of the box. The surface of these cracks is rough, with their asperities influenced by the layering of the hemihydrate.

The vertical fractures initially form as tensile fractures but deeper in the box they may develop into shear fractures (Figs. 10c and 11b). A complex set of en-echelon faults and both down- and upward propagating fractures formed more towards the middle of the box resulting in the development of Through Going Structures (TGS; Figs. 10c and d, 11b and c and 12, key 2) that run from the bottom of the box to the surface. Once formed, these TGS accommodate the bulk of the deformation (Fig. 10e). New TGS can form by overstepping of faults and form fault arrays. These new TGS form on the hangingwall side of the older TGS. The average dip of a TGS is 68° up to roughly 5–7 cm below the surface. Here it generally connects to an older Mode I fracture, and becomes roughly vertical. The master faults have dips of 60°, thus the central block of hemihydrate gets increasingly unsupported with progressive deformation. Antithetic fractures form within this block (Fig. 12, key 3). Newer antithetic fractures form farther from the centre of the box as deformation continues.

Though the overall average dip of the TGS is 68°, local dips between 45° and 90° have been observed within single faults. Overturned fractures form in some cases (Fig. 12, key 4a), and local decrease of the dip (Fig. 12, key 5, see interpreted fault segment in white) can also occur.

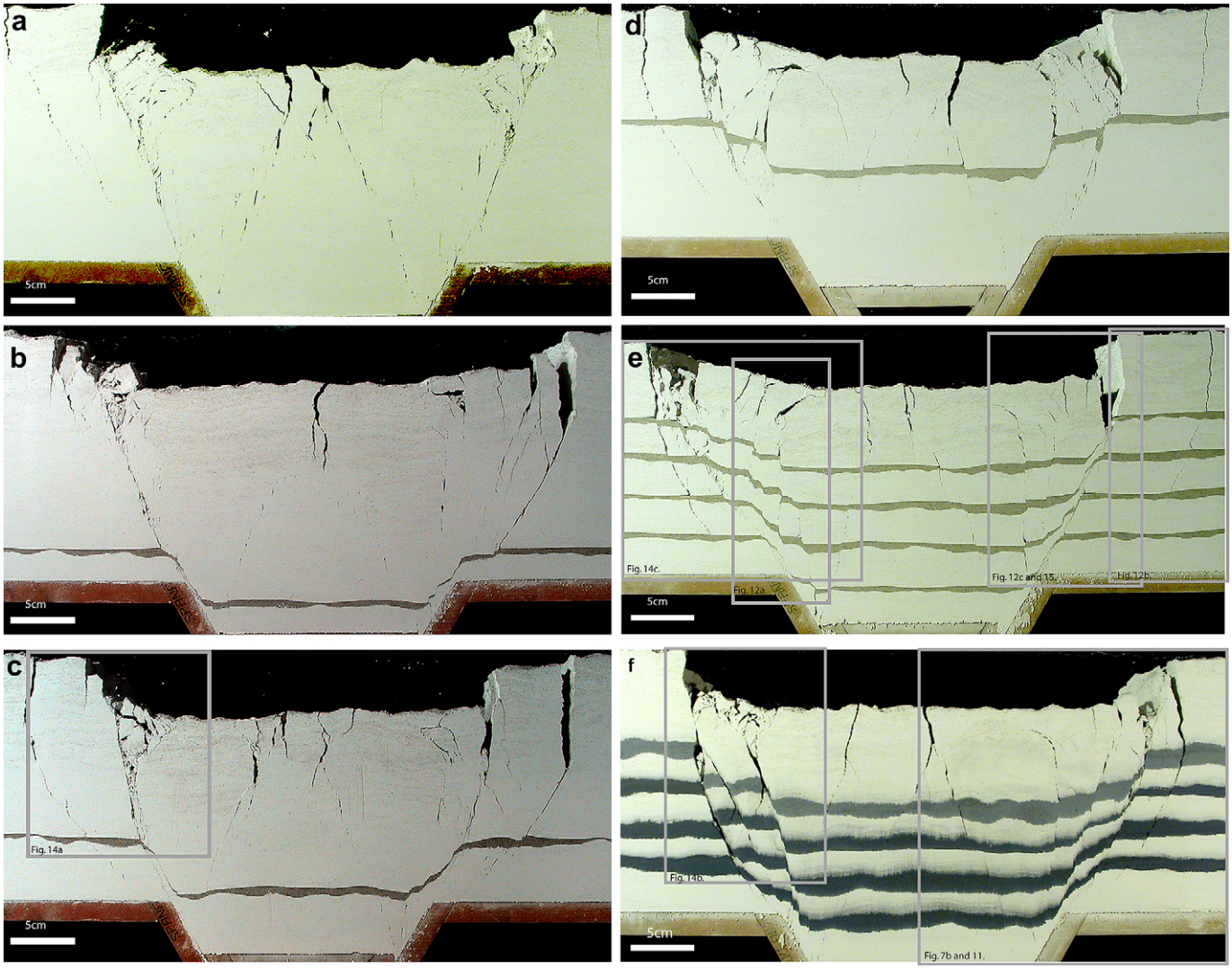

Fig. 9. Overview of the different experiments. All photos are taken after a horizontal elongation of about 7%. The initial length of the model is 70 cm, and the hemihydrate column is 20 cm high. In experiment 1 (a), only hemihydrate was used. Experiment 2 (b) has a 4 mm thick sand layer at 2 cm from the bottom. In experiment 3 (c) a 4 mm sand layer was included at 5 cm from the bottom. In experiment 4 (d) 4 mm sand layer was included 10 cm from the bottom. In experiment 5 (e) 4 mm thick sand layers were included at 3, 6.5, 10 and 13.5 cm from the bottom. In experiment 6 (f), four 1 cm layers of hemihydrate graphite mixture are included at 3, 6, 9 and 12 cm from the bottom. Movies of selected experiments can be found at http://www.ged.rwth-aachen.de and http://www.ged.rwth-aachen.de/Ww/people/heijn/heijn_index.html.

When the dip increases along faults, continued deformation and fault slip can result in dilatation of these segments and the opening of fault cavities. These structures are typically not higher than 1 cm (Fig. 12, key 4, and Fig. 13a and b). In some cases, the roof of fault cavities fails and fragments partially fill the dilatant fault segments (Fig. 12, key 4a and compare Fig. 13b1 and b2).

When a TGS connects to a Mode I fracture, further shearing at depth results in a clear height difference between the two sides of the vertical fracture. Cliffs develop on the footwall side of the fracture (Fig. 12, key 9). These cliffs reach maximum heights of 7 cm in our experiments, in agreement with our experiments to characterize material properties (Section 2.1.4). Interaction between faults near the surface leads to the formation of a rotating, wedge shaped block (see Fig. 13a and b). Progressive deformation disintegrates these rotating blocks to form rubble zones (Fig. 13a3 and b3) at the surface. Small hemihydrate fragments, and in some experiments sand grains, move down the open fractures forming a fault breccia in the roughly 0.8 cm wide deformation zone. Here the fragments are further reduced in size by continued fault movement and also entrain pieces of the fault wall.

6.4. Later deformation in experiments with sand layers

The sand layers in our experiments form a weaker layer in the stratigraphy. As a result, they can act as "decoupling" layers for deformation. Fault segmentation due to the sand layers can result in dip changes between the layers. In experiment 5 (Figs. 9e and 13c) the developing TGS (Fig. 13c2) show a distinct reduction of dip between the lowest and second lowest sand layer, when compared with the overall dip of the structure. The resultant 'ramp–flat–ramp'-type of fault geometry creates a fault monocline at the surface.

The inclusion of sand layers in experiments can also lead to the development of relatively wide shear zones (Fig. 9b–e). Fig. 14 shows a series of images late in the development of experiment 5, where the hemihydrate and sand layers are sheared in a 0.7 cm wide deformation zone, which still shows some dilatancy, particularly along the lower boundary. The sand layers remain continuous in the fault zone. Fig. 14c shows mechanical mixing of hemihydrate and sand into a fully developed fault gouge, forming a geometry very similar to clay smears (cf. Fulljames et al., 1997;

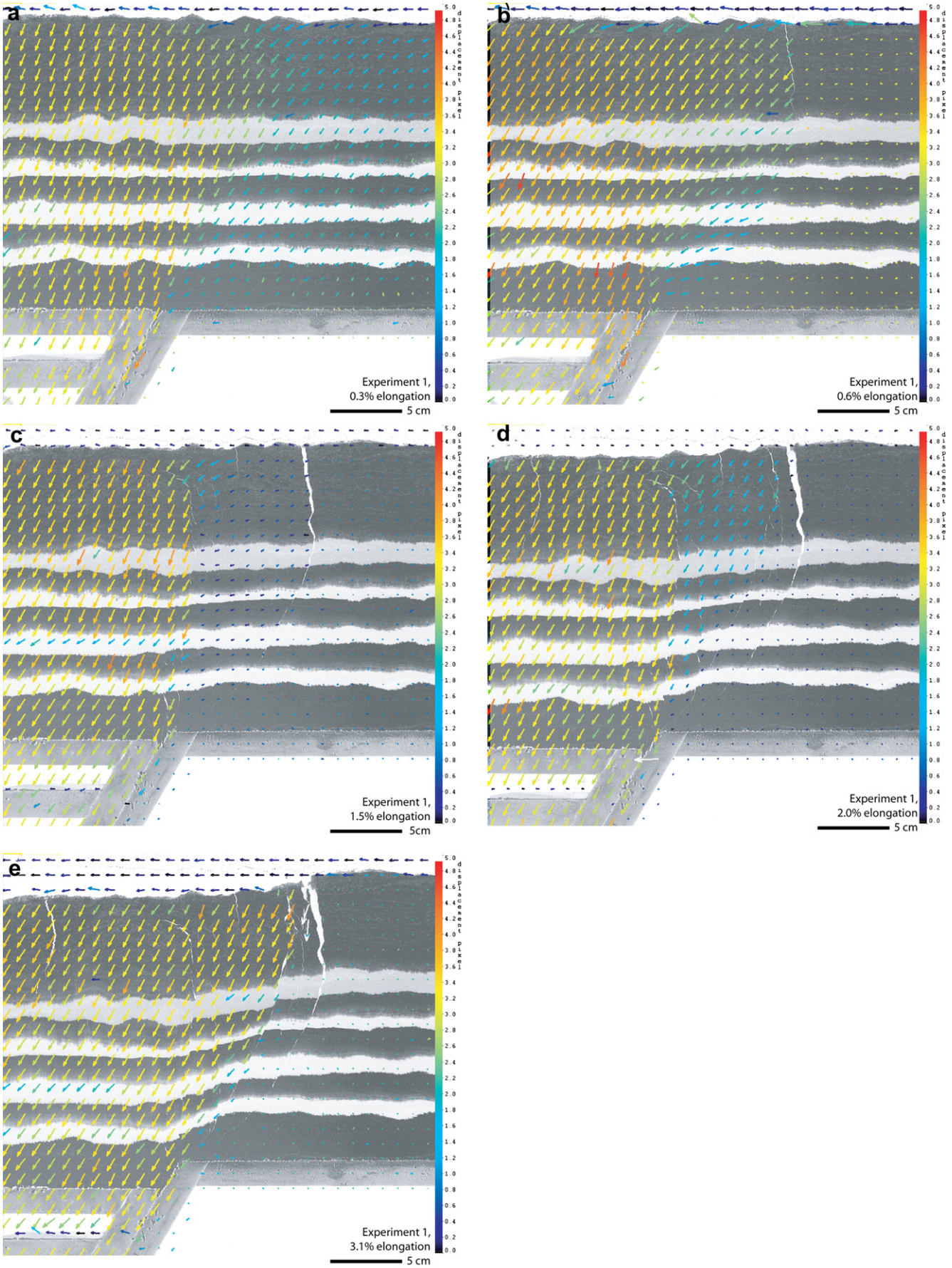

Fig. 10. Evolution of a fault array, visualized using PIV. See text for discussion. Images from experiment 6, note that the greyscale colour bar of the background image is inverted, and that vector lengths are multiplied by 14. The reference frame is fixed to the right basement block.

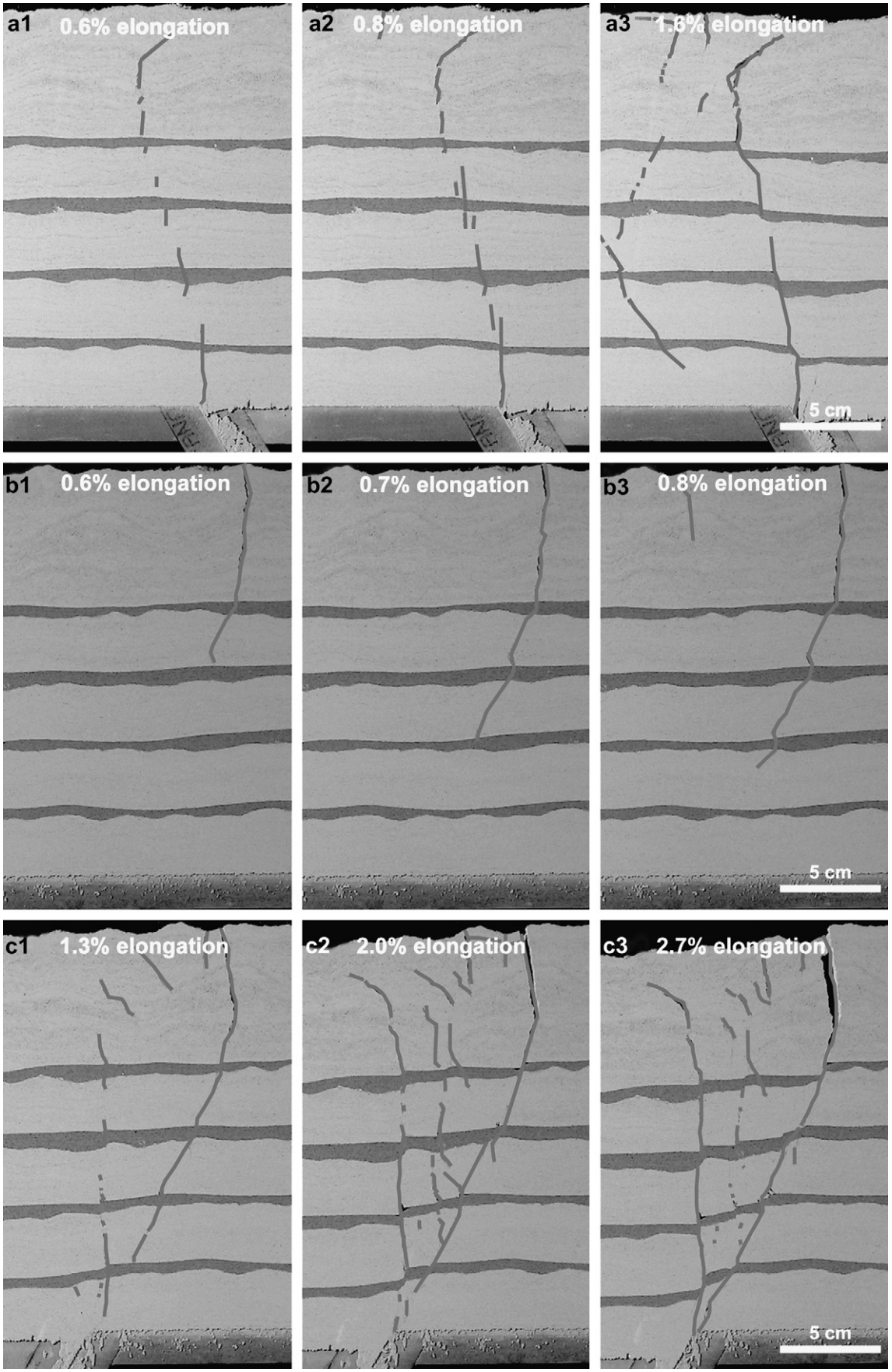

Fig. 11. The effects of decoupling sand layers on the initial deformation. All images are from experiment 5. (a) The formation of a segmented fault from multiple smaller fractures, which formed on the sand/hemihydrate transitions. (b) Formation of a downward propagating segmented fracture. Note the curving of the fracture when it crosses a sand layer. (c) The formation of a segmented fault array. Note how the number of visible fractures reduces with progressive deformation. Some of the fractures are closed with progressive deformation.

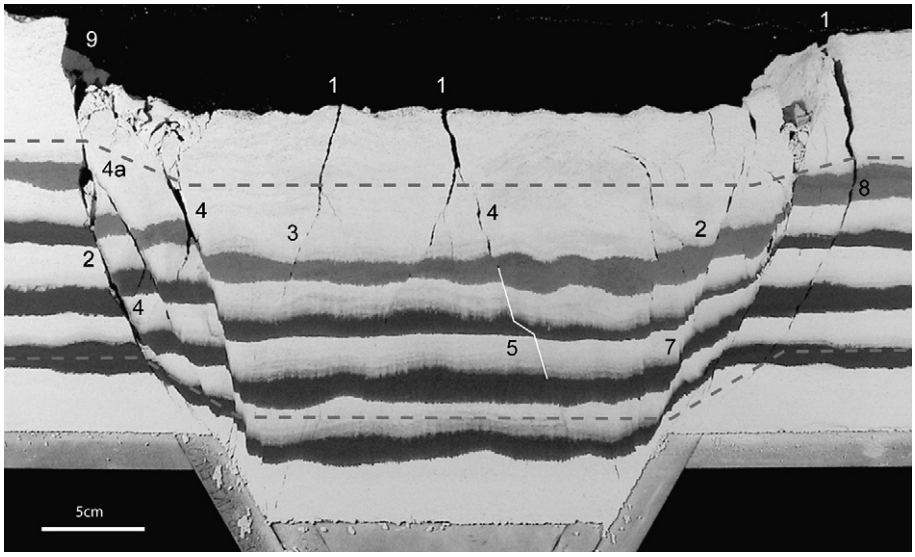

Fig. 12. Overview of structures observed in the experiments. See text for the keys. The image is frame 100 of experiment 6 (horizontal elongation = 7%). Stippled lines indicate transitions between a zone of pure Mode I, the zone of dilational shear faulting and the zone of non-dilational shear faulting (see also Fig. 15).

Lehner and Pilaar, 1997; Van der Zee et al., 2003; Van der Zee and Urai, 2005; Schmatz, 2006).

6.5. The effects of mechanical stratigraphy and material properties

In general, comparing the results of all experiments (Fig. 9), the inclusion of a mechanical stratigraphy of any kind leads to an increase of the complexity of the structures in the model. An obvious difference between experiments 5 and 6 is the inclusion of softer and slightly stronger layers respectively. Nevertheless, the results of these models are similar to each other in their difference to experiment 1. The inclusion of mechanical stratigraphy has resulted in a wider zone of deformation in both cases. While the uniform setup used in experiment 1 resulted in a relatively simple structure with a single Through Going Structure on each side of the central fault block, the inclusion of a single sand layer (experiments 2–4) or of several sand or gypsum/graphite layers (experiments 5 and 6) leads to wider deformation zones and multiple faults being active at the same time (see also Figs. 10–13).

All models can be subdivided in three structural zones (Figs. 12 and 14). The upper 6–7 cm of the models are dominated by near-vertical Mode I tensile fractures. The lowest 5–7 cm show non-dilatant shear faults, and in the transition zone the shear fractures can form hybrid, dilatant fault cavities. These zones are related to the compaction related increase of material strength as well as the increase of the principle stresses with depth (Fig. 15). In Fig. 15a, cohesion, tensile strength and angle of internal friction at different depths are calculated using the material characterisation of the powder, described above. The magnitude of σ_1 is calculated using:

$$\sigma_1 = \rho g h$$

Here ρ is the powder density, g is the gravity acceleration and h is the depth in the box. The horizontal stress (σ_3) at rest is calculated using the Jaky Equation for K_0 (Jaky, 1944; Lambe and Whitman, 1969; Muir Wood, 1990). The shape of the pore collapse surface (Roscoe surface in p/q diagrams) in Fig. 15a is an approximation, as this surface is not characterised in our experiments. A material at rest, compacting under its own weight touches this surface near σ_1 (Lambe and Whitman, 1969; Muir Wood, 1990). However, a stress of 650 Pa is required to start permanently compacting hemihydrate (Fig. 3). The Roscoe surface is therefore moved to the right along the normal stress axis at depths of 4 cm and 10 cm.

The Mohr circles at failure are constructed by keeping σ_1 fixed, while σ_3 is decreased (arrow in Fig. 15a). With increasing depth, σ_1 and material strength increase, but the overburden stress increases roughly ten times faster than cohesion and fifty times faster than tensile strength. In Mohr diagrams (Fig. 15a), the failure modes thus moves out of the tensile failure field and into the field of hybrid and later shear failure with increasing normal stress. The models are in agreement with this; a Mode I fracture propagating down from the surface will change dip and failure mode as it moves from the tensile failure field into the hybrid failure field. This is shown for example in Fig. 12 (key 8). The depth where this change occurs corresponds to the maximum height of an unsupported hemihydrate column, 6–7 cm and the cliff height. Below a depth of roughly 14 cm fault cavities no longer occur, as the Mohr failure moves into the non-dilatant shear failure field.

7. Discussion

7.1. Material characterisation and model set up

One of the most important results from this work is the characterisation of the dependence of material properties on compaction, and the failure mode transitions in the experiments corresponding to this. Galland et al. (2006) also observed that compaction of the fine grained powder increases its cohesion but this effect was not quantified. Sibson (2003) notes that the maximum sustainable height of an open fracture is proportional to the tensile strength and the cohesion of the material. We used this relation to compare our hemihydrate to the cohesive material of Galland et al. (2006). A doubling of the maximum sustainable height of open fractures does not correspond to a doubling of the tensile strength and cohesion in this case. We propose that in future experiments using cohesive materials, maximum sustainable fracture height is always included in the material characterisation protocol.

Compared to the models of Holland et al. (2006), our models' layering is significantly more uniform due to the use of the new sieving method. As a result, the structures developed in the models

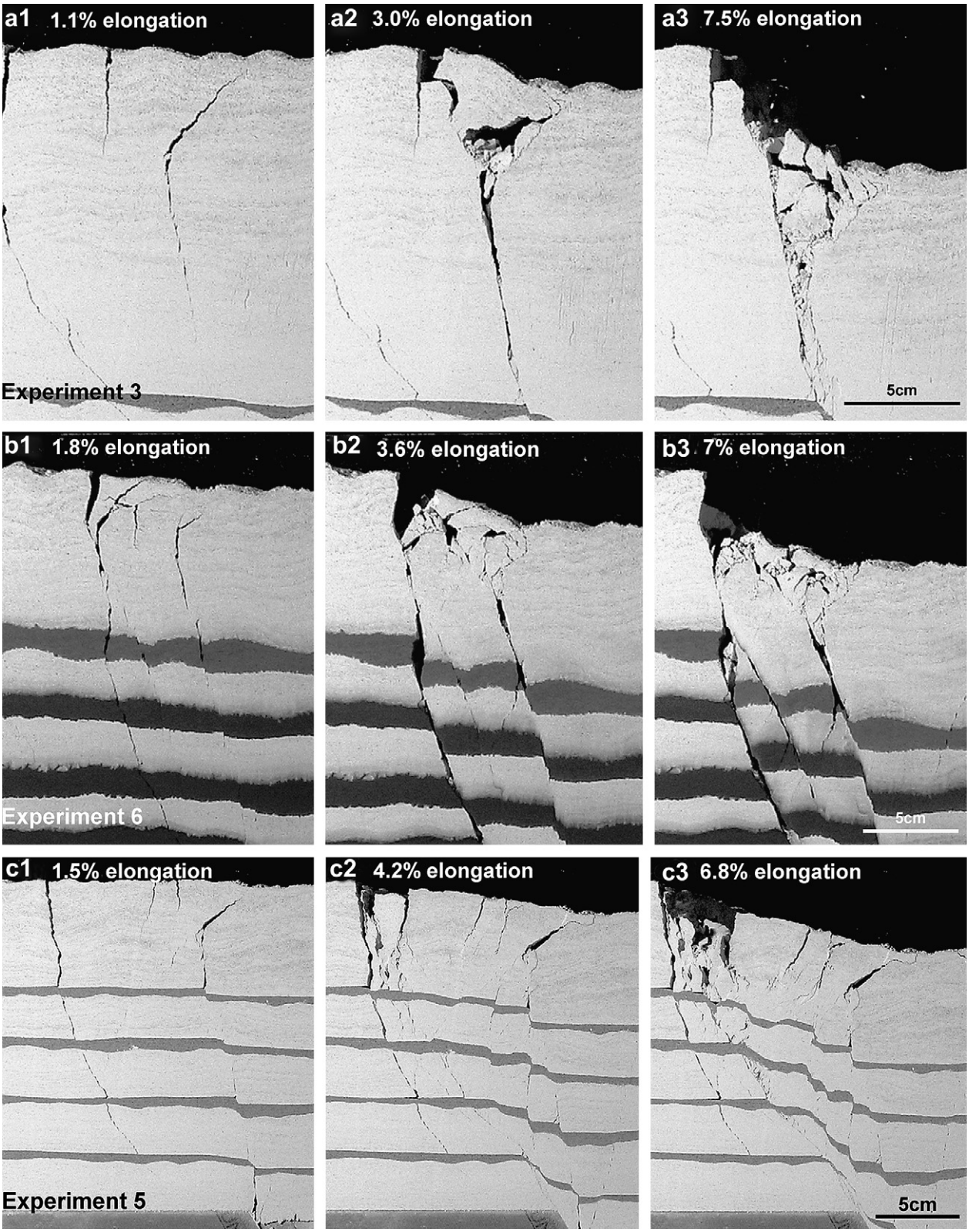

Fig. 13. (a) Development of a rotating block (a1 and a2) and the disintegration of this block (a3) with increasing deformation. Fragments move down the fracture, forming a fault breccia and gouge, while at the surface a rubble zone and cliff are formed. Images from experiment 3. (b) Development of dilational jogs on the mechanical stratigraphy (b1 and b2). Also shown is the gravitational collapse of the roof of the jog in b3. Images from experiment 6. (c) Development of a monocline, as a decrease in fault-dip (between lowest and second lowest sand layers) deforms the overlying material. Also note the shearing of the sand layers across the fault, and the antithetic faults in the top of figure c3. Images from experiment 5.

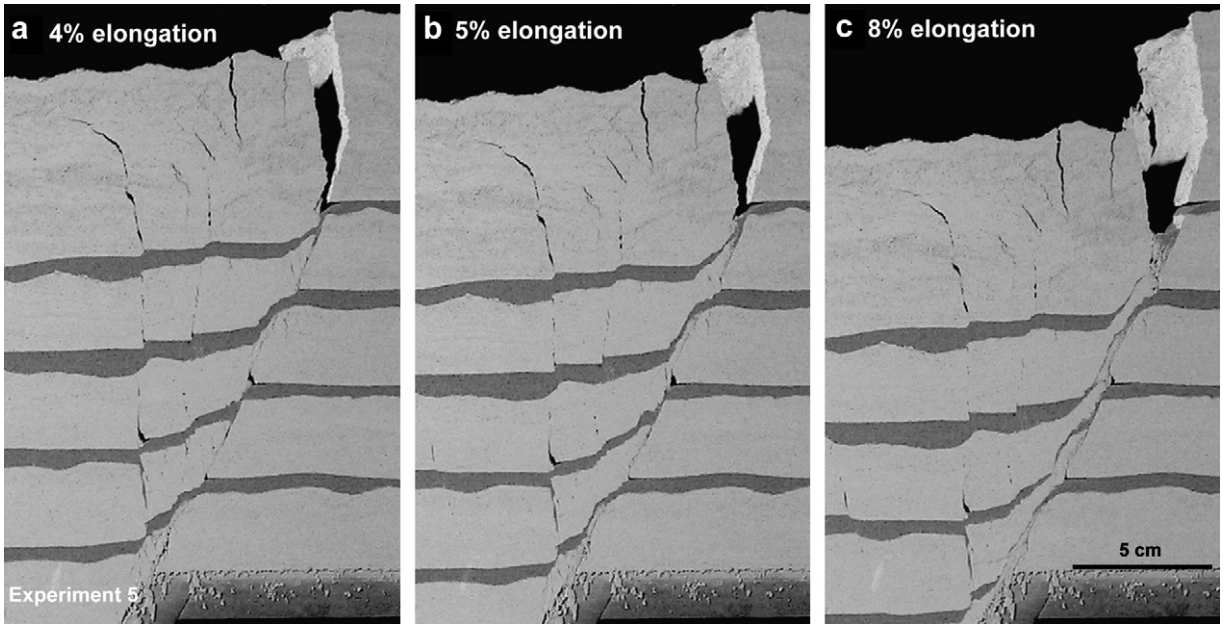

Fig. 14. The formation of smeared sand layers with progressive elongation. These smears are very similar to clay smears (Fulljames et al., 1997; Lehner and Pilaar, 1997; Van der Zee et al., 2003; Van der Zee and Urai, 2005; Schmatz, 2006).

presented here are much simpler than those of Holland et al. (2006). A similar observation is made when comparing the results of experiments 1, 5 and 6 (Fig. 9a, e and f), where the inclusion of either sand or hemihydrate/graphite mixture interlayers leads to the development of a much wider and more complex deformation zone. Even small competence differences in these models lead to changes in the structural style.

The closure of fractures in hemihydrate, which is observed by the reduction of interpreted fractures for example in Fig. 11a and c, implies that the final geometry of any model may not always represent its full structural history and complexity.

7.2. Elastic behaviour prior to brittle failure

Materials like sand and hemihydrate are expected to show pronounced nonlinear elastic behaviour prior to brittle failure (Lambe and Whitman, 1969; Muir Wood, 1990; Patton and Fletcher, 1995). In Fig. 10a the displacement field shows a continuous field without brittle features, interpreted as predominantly elastic, reflecting the initial stress field. To test this, the horizontal strain (e_{xx}) was calculated along the surface of the model, from the PIV data. This value is 0.26%, which corresponds well to the measured strain of 0.2% at the onset of plasticity in our shear experiments.

7.3. Model evolution compared with dilatant fault zones in carbonates

7.3.1. Initial brittle deformation

Sibson (1996) inferred that open fractures can form without high pore fluid pressures at depths between 0 and 3 km in strike-slip and normal faulting settings, provided the rocks have sufficient cohesion. The dilational jogs described by Ferrill and Morris (2003) are assumed to be formed at depths smaller then 1 km. Our scaling ratio suggests that the hybrid failure zone (between 7 and 14 cm) corresponds to a depth range of 600–1400 m in nature.

Micarelli et al. (2005) observe initial deformation by Mode I fracturing in mainly mudstone and fine calcarenite alternations with thin clayey interlayers in the SE-Basin, France. Two types of Mode I fractures are observed, initially randomly distributed vertical fractures form throughout the entire rock mass, while in a later stage en-echelon fractures form in shear bands at relatively high P/T conditions ($T > 120\,^{\circ}C$; depth $\sim$2.9–3.6 km). In another outcrop with the same rocks, but deformed at lower P/T conditions ($T < 90\,^{\circ}C$; depth $\sim$1.5–2 km), the second stage of deformation is dominated by flexural extensional fractures that form a couple of upward and downward propagating fractures within single layers in the outcrop.

The first type of Mode I fractures is not observed in this study. The scaling ratio suggests that they would be smaller than the hemihydrate clusters. En-echelon Mode I fractures in shear bands are observed in Figs. 10c and 11a and c, while upward and downward propagating pairs of flexural extension faults are observed in Figs. 10c and 11b. These two types of structures form in a single experiment at roughly the same elongations as in nature, although the outer-arc flexural bending fractures in our experiments form over the entire thickness of the model, and not within single layers. These structures form in outcrop at widely different P/T conditions (Micarelli et al., 2005). This may be the result of the absence of reactive pore fluids in our experiments.

7.3.2. Later structures

In some cases fragments in our experiments travel down into the open fault and form a fault breccia in a wide deformation zone (Fig. 13a3). These zones are similar to the fault cores described for example by Billi et al. (2003) and Billi and Storti (2004). In these examples the fault zone consists of damage zones on both sides, with a master fault on side of the fault core, while on the other side the transition from host rock to the damage zone is more gradual. This level of detail is not present in our models. Using the scaling relations from this study, the displacement in the fault zone described by Billi and Storti (2004) is about 400% of those in our models. The fault core development model of Billi et al. (2003) describes that the fault core material stems from the damage zone directly adjacent the fault, and no vertical material transport along the fault takes place. These fault cores are not dilatant, leaving no room for vertical gravity-driven transport. Observations from the

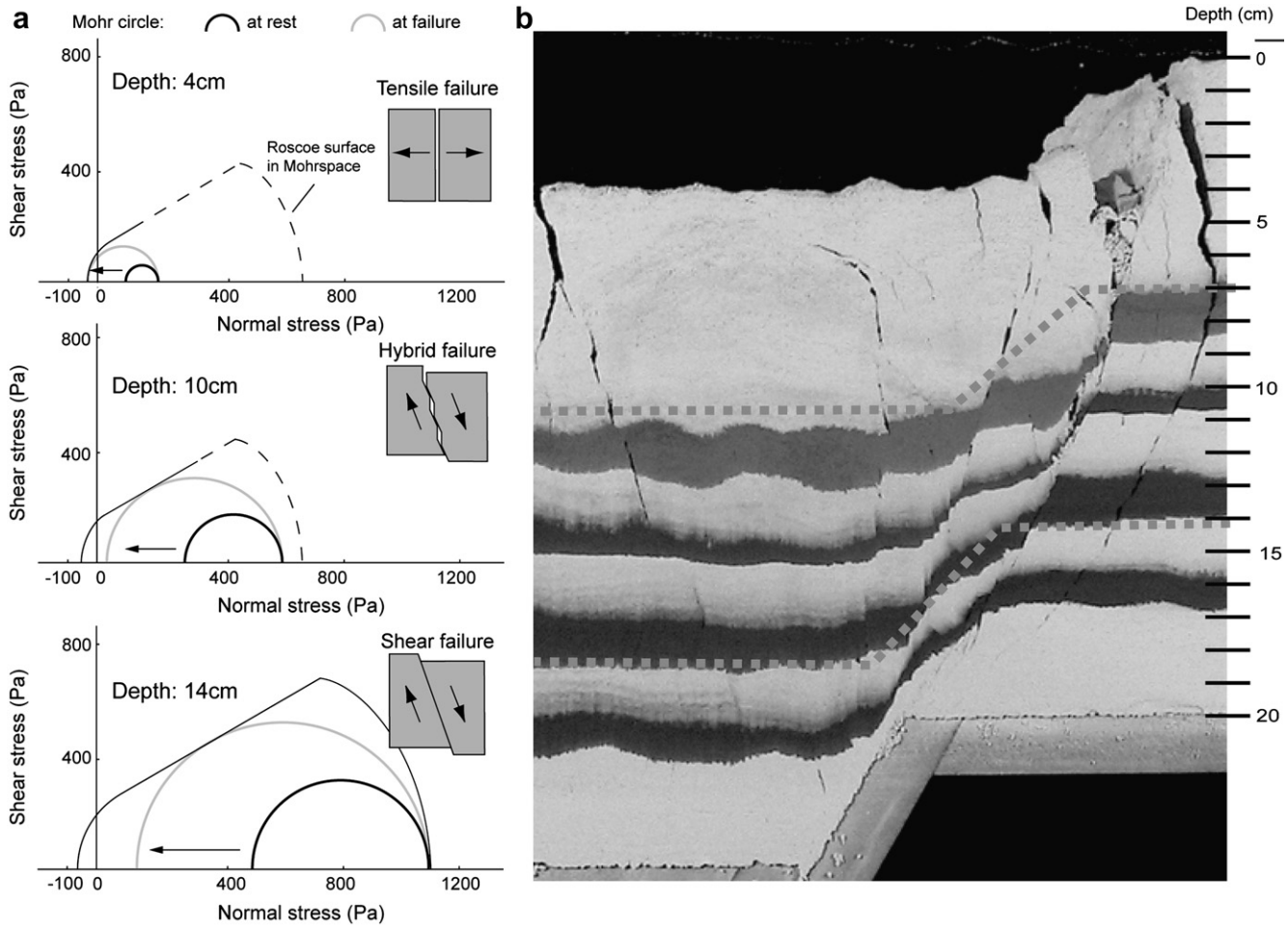

Fig. 15. (a) Mohr circles and failure envelopes at different depths in the experimental box. The diagram is constructed using the empirical relations from this study. Mohr circles "at rest" (showing the state of stress at the start of deformation) evolve (arrow) during deformation by decreasing σ_3 until they touch the failure envelopes at failure. The increase of strength due to the "pseudo-burial" effect is indicated with the stippled failure envelopes. At different depths in the box, the Mohr circle touches the failure envelope at different locations, which correspond to the different "structural zones" shown in Fig. 14b.

dilational normal faults in Jebel Hafeet do however show that vertical transport of material in fault zones (Fig. 1a) does occur. In a different lithology, the basalts of the Ethiopian Rift show dilatant fault zones filled with weathered debris from the fault scarps (Acocella et al., 2003), as do the open fractures in the Koa'e fault zone (Big Island, Hawaii), where rotating blocks (Fig. 13a) were also observed (Holland et al., 2006).

Fig. 13c shows the development of a monocline as the result of a "ramp–flat" structure in the main fault of the model. In natural carbonates however, the compression exerted on the hangingwall above this structure would most likely result in the development of stylolites. The exclusion of pore fluid in our models does not allow these types of structures to form. Also, the closing of fractures in Fig. 11c could be accompanied by dissolution in nature, while natural open fractures tend to close and regain their strength over time due to mineral precipitation.

In Fig. 14, the softer sand layers are sheared into the fault zone in a geometry which is very reminiscent of clay smears. The development of clastic smears is significant in carbonate hydrocarbon reservoirs, as the clay smear development has pronounced effects on the sealing capacity of faults (Fulljames et al., 1997; Lehner and Pilaar, 1997; Van der Zee et al., 2003; Van der Zee and Urai, 2005; Schmatz, 2006). The inclusion of even minor amounts of clay-rich material in the dilatant fault segments (Fig. 1a), will decrease permeability of the fault zone. As observed in the field (Fig. 1b), sedimentation of clay from elsewhere in the sequence in open fractures is a powerful process of resealing faults in carbonates, completely different from previously recognized mechanisms of clay-enrichment in fault zones.

7.3.3. Mechanical stratigraphy and the evolution of carbonate fault zones

Ferrill and Morris (2003) describe changing material properties as one of the mechanisms for variation in fault-dip and failure mode. If a fault cuts through a material with a higher friction angle, the local dip of the fault will be steeper than the overall dip (Wallace, 1861; Dunham, 1948, 1988; Ramsay and Huber, 1987; Peacock and Zhang, 1993; Mandl, 2000; Sibson, 2000; Ferrill and Morris, 2003; Schöpfer et al., 2007a). Continued fault slip will open these steeper sections to form dilatational jogs (e.g. Fig. 12, keys 4 and 6 and Fig. 13b; Ferrill and Morris, 2003). These dilatant fault segments occur in the hemihydrate, but not in sand layers. The occurrence of these dip changes in models with pure hemihydrate is most likely the result of local changes in the density (and associated changes in mechanical properties) as a result of non-uniform sieving. In layered models, the dip changes and associated dilational jogs in Fig. 13b are interpreted to be related to the transitions between mixed and hemihydrate layers.

The evolution of the fault in Fig. 11a is the result of vertical Mode I fault segment linkage in a shear band. Vertical fault segment linkage

in carbonates was described by Childs et al. (1996), in the marl/clay sequences of the Flamborough Chalk Formation of Yorkshire, UK. Childs et al. (1996) and Schöpfer et al. (2007b,c) infer that in layered sequences individual fault segments are initiated as separate structures forming in the brittle layers, which later coalesce. A similar evolution is shown in Fig. 11a, but here the fracture segments are not confined to the weaker sand layers but also slightly extend into the hemihydrate powder. Shear dilatant behaviour in the sand, combined with the relatively high competence contrast between the layers could be a reason for the local stress concentrations and the formation of cracks in the hemihydrate.

7.3.4. Implications and applications to natural carbonate fault zones

Dilational deformation structures cannot only increase permeabilities in "tight" reservoirs and thus promote hydrocarbon production, but are also associated with exploration and production problems such as "early water production" and loss or gain of circulation fluids during drilling (Arnott and Van Wunnik, 1996; Sapra, 1997; Van Konijnenburg et al., 2000; Kerans, 2002; Ehrenberg and Nadeau, 2005; Casabianca et al., 2007).

Rare surface outcrops of dilatant normal faulting in carbonates such as those observed at Jebel Hafeet (Fig. 1) show that deformation within a shallow extensional regime creates massive asperities and large dilatant structures. These can reach sizes exceeding several decimetres leading to extreme focussing of fluid flow, and perhaps initiation of caves. Although the formation of caves is often not explicitly discussed, there are some examples of published fault-cave-surveys where the effects of open faulting and dilatant behaviour of competent carbonates could be related to cave formation. In the Polish Flysch Carpathians, the top parts of a series of caves formed along faults consist of a series of vertically positioned rooms up to a depth of 15 m (Margielewski and Urban, 2003). At the point where the fault crosses from the carbonate cemented sandstone into the underlying shales, the dip changes, and open caverns are no longer present. The absence of slickensides on the walls of the cave suggested to the authors that the opening can be related to the down-dip movement observed across the fault, very similar to the development of open fractures in at the surface of our experiments.

The formation of the rooms (up to depths of 60 m) of the Barrenc du Paradet cave in carbonates of the French Pyrenees is interpreted by Gilli et al. (1999) to result from dilatant movement along shallower dipping segments of an oblique-reverse fault. This mechanism is the opposite of the formation of dilational jogs along steeper sections of a normal fault. This cave experienced significant karstification after faulting.

8. Conclusions

- The tensile strength and cohesion of hemihydrate increase during compaction, while the angle of internal friction does not. This change in material properties results in the development of three structural zones in our models.
- The determination of the maximum sustainable height of vertical walls is a quick way to compare the relative tensile strengths of model materials.
- The inclusion of decoupling sand layers or gypsum/hemihydrate layers results in a segmented growth of main fractures and a wider, more complex fault zone.
- Gravity-driven downward transport of fragments in dilatant parts of a fault zone is an important process for the formation of fault breccia.
- The softer sand layers can be sheared along the fault zone during progressive deformation, indicating that the clay smear similar process of clastic smearing can operate in carbonate reservoirs.
- The presence of dilatant fault segments in the crust can explain the formation of some cave systems, as well as problems in exploration and production of hydrocarbons in carbonates, such as early water production.

Acknowledgements

This study was sponsored by Shell Abu Dhabi and greatly benefited from input by Pascal Richard (Petroleum Development Oman). The authors would like to further thank Professor Zimmerman and Sabine Dünisch from the Lehrstuhl für Pharmazeutische Technologie of the University of Würzburg for the tensile strength measurements. Franz Grümmer, Werner Kraus and Manfred Debye (RWTH Aachen) are thanked for their technical assistance. Special thanks to Joyce Schmatz (RWTH Aachen) for her discussions on the PIV software and analogue modelling, Steffen Abe (RWTH Aachen) for discussions on Mohr space and Dipl.-Ing. Gisa Kleine Vennekate (RWTH Aachen) for discussing the failure envelopes. This paper benefited considerably from the critical review by Nicola de Paola, the editors Fabrizio Agosta and Emanuele Tondi, Professor Blenkinsop and an anonymous reviewer. Finally H.W. Van Gent would like to personally thank his former tutor Dr Hans de Bresser (Utrecht University) who encouraged the author to start this research in Aachen as an MSc project.

References

Acocella, V., Korme, T., Salvini, F., 2003. Formation of normal faults along the axial zone of the Ethiopian Rift. Journal of Structural Geology 25, 503–513.
Adam, J., Urai, J.L., Wieneke, B., Oncken, O., Pfeiffer, K., Kukowski, N., Lohrmann, J., Hoth, S., Van der Zee, W., Schmatz, J., 2005. Shear localization and strain distribution during tectonic faulting-new insights from granular-flow experiments and high-resolution optical image correlation techniques. Journal of Structural Geology 27, 283–301.
Agosta, F., Aydin, A., 2006. Architecture and deformation mechanism of a basin-bounding normal fault in Mesozoic platform carbonates, central Italy. Journal of Structural Geology 28, 1445–1467.
An, L.-J., 1998. Development of fault discontinuities in shear experiments. Tectonophysics 293, 45–59.
Angelier, J., Bergerat, F., Dauteuil, O., Villemin, T., 1997. Effective tension–shear relationships in extensional fissure swarms, axial rift zone of northeastern Iceland. Journal of Structural Geology 19, 673–678.
Arnott, S.K., Van Wunnik, J.N.M., 1996. Targeting infill wells in the densely fractured Lekhwair Field, Oman. GeoArabia 1, 405–416.
Baldassarre, A., DeLucia, M., Nesi, P., Rossi, F., 2001. A vision-based particle tracking velocimetry. Real-Time Imaging 7, 145–158.
Bekendam, R.F., 1998. Pillar Stability and Large-scale Collapse of Abandoned Room and Pillar Limestone Mines in South-Limburg, the Netherlands. Ph.D. thesis. Technische Universiteit, Delft.
Billi, A., Salvini, F., Storti, F., 2003. The damage zone-fault core transition in carbonate rocks: implications for fault growth, structure and permeability. Journal of Structural Geology 25, 1779–1794.
Billi, A., Storti, F., 2004. Fractal distribution of particle size in carbonate cataclastic rocks from the core of a regional strike-slip fault zone. Tectonophysics 384, 115–128.
Birch, F.F., 1966. Compressibility, elastic constants. In: Clack, S.P. (Ed.), Handbook of Physical Constants, revised ed.The Geological Society of America Memoir 97 The Geological Society of America.
Borkhataria, R., Aigner, T., Poppelreiter, M.C., Pipping, J.C.P., 2005. Characterization of epeiric 'layer-cake' carbonate reservoirs; Upper Muschelkalk (Middle Triassic), the Netherlands. Journal of Petroleum Geology 28, 119–146.
Breesch, L., Swennen, R., Vincent, B., 2009. Fluid flow reconstruction in hanging and footwall carbonates: compartmentalization by Cenozoic reverse faulting in the Northern Oman Mountains (UAE). Marine and Petroleum Geology 26, 113–128.
Buiter, S.J.H., Babeyko, A.Y., Ellis, S., Gerya, T.V., Kaus, B.J.P., Kellner, A., Schreurs, G., Yamada, Y., 2006. The numerical sandbox: comparison of model results for a shortening and an extension experiment. In: Buiter, S.J.H., Schreurs, G. (Eds.), Analogue and Numerical Modelling of Crustal-Scale Processes. Geological Society, London, Special Publications, vol. 253, pp. 29–64.
Bussolotto, M., Benedicto, A., Invernizzi, C., Micarelli, L., Plagnes, V., Deiana, G., 2007. Deformation features within an active normal fault zone in carbonate rocks: the

Gubbio fault (Central Apennines, Italy). Journal of Structural Geology 29, 2017–2037.
Cailleau, B., Walter, T.R., Janle, P., Hauber, E., 2003. Modelling volcanic deformation in a regional stress field: implications for the formation of graben structures on Alba Patera, Mars. Journal of Geophysical Research 108, 1–18.
Callari, C., Auricchio, F., Sacco, E., 1998. A finite-strain Cam-clay model in the framework of multiplicative elasto-plasticity. International Journal of Plasticity 14, 1155–1187.
Cardozo, G.L., Bada, G., Lankreijer, A., Nieuwland, D., 2002. Analogue modelling of a prograding strike-slip fault: case study of the Balatonfo fault, western Hungary. In: EGU Stephan Mueller, Special Publication Series, vol. 3, pp. 217–226.
Casabianca, D., Jolly, R.J.H., Pollard, R., 2007. The Machar oil field: waterflooding a fractured chalk reservoir. In: Lonergan, L., Jolly, R.J.H., Rawnsley, K., Sanderson, D.J. (Eds.), Fractured Reservoirs. Geological Society, London, Special Publications, vol. 270, pp. 171–191.
Childs, C., Nicol, A., Walsh, J.J., Watterson, J., 1996. Growth of vertically segmented normal faults. Journal of Structural Geology 18, 1389–1397.
Cloos, H., 1930. Zur experimentellen Tektonik. Geologische Rundschau XXI, 355–367.
Crider, J.G., Peacock, D.C.P., 2004. Initiation of brittle faults in the upper crust: a review of field observations. Journal of Structural Geology 26, 691–707.
Dunham, K.C., 1948. Tyne to Stainmore, Geology of the Northern Pennine Ore field. In: Memoirs of the Geological Survey of Britain, vol. 1 London.
Dunham, K.C., 1988. Pennine mineralization in depth. Proceedings of the Yorkshire Geological Society 47, 1–12.
Ehrenberg, S.N., Nadeau, P.H., 2005. Sandstone vs. carbonate petroleum reservoirs: a global perspective on porosity–depth and porosity–permeability relationships. AAPG Bulletin 89, 435–445.
Ferrill, D.A., Morris, A.P., 2003. Dilational normal faults. Journal of Structural Geology 25, 183–196.
Fulljames, J.R., Zijerveld, L.J.J., Franssen, R.C.M.W., 1997. Fault seal processes: systematic analysis of fault seals over geological and production time scales. In: Moeller-Pedersen, Koester, A.G. (Eds.), Hydrocarbon Seals. NPF, Special Publications, vol. 7, pp. 51–59.
Galland, O., Cobbold, P.R., Hallot, E., de Bremond d'Ars, J., Delevaud, G., 2006. Use of vegetable oil and silica powder for scale modelling of magmatic intrusion on a deforming brittle crust. Earth and Planetary Science Letters 243, 786–804.
Gilli, E., Levreet, A., Sollogoub, P., Delange, P., 1999. Research on the February 18, 1996 earthquake in the caves of Saint-Paul-de-Fenouillet area (eastern Pyrenees, France). Geodinamica Acta 12, 143–158.
Gipsindustrie, 2003. Gipsdatenbuch. Forschungvereinigung der Gipsindustrie e.V., Darmstadt (Germany). www.gips.de.
Griffith, A.A., 1921. The phenomenon of rupture and flow in solids. Philosophical Transactions of the Royal Society of London Series A 221, 163–198.
Hancock, P.L., 1985. Brittle microtectonics; principles and practice. Journal of Structural Geology 7, 437–457.
Hoek, E., 2007. Practical Rock Engineering Availible online at: http://www.rocscience.com/hoek/pdf/Practical_Rock_Engineering.pdf.
Holland, M., Urai, J.L., Martel, S., 2006. The internal structure of fault zones in basaltic sequences. Earth and Planetary Science Letters 248, 286–300.
Horsfield, W.T., 1977. An experimental approach to basement-controlled faulting. Geologie en Mijnbouw 56, 363–370.
Hubbert, M.K., 1937. Theory of scale models as applied to the study of geological structures. Geological Society of America Bulletin 48, 1459–1520.
Jaky, J., 1944. The coefficient of earth pressure at rest. Journal of the Society of Hungarian Architects and Engineers 22, 355–358.
Jones, M.E., Addis, M.A., 1986. The application of stress path and critical state analysis to sediment deformation. Journal of Structural Geology 8, 575–580.
Jones, M.E., Leddra, M.J., Goldsmith, A.S., Yassir, N., 1991. Chapter 2: mechanisms of compaction and flow in porous sedimentary rocks. In: Cosgrove, J., Jones, M.E. (Eds.), Neotectonics and Resources. Bellhaven Press, London & New York, pp. 17–42.
Kerans, C., 2002. Evolving technologies and opportunities in carbonate systems. AAPG Bulletin 86, 193.
Lambe, T.W., Whitman, R.V., 1969. Soil Mechanics. John Wiley & Sons, Inc., New York.
Lehner, F.K., Pilaar, W.F., 1997, The emplacement of clay smears in synsedimentary normal faults: inferences from field observations near Frechen, Germany. In: Møller-Pedersen, P., Koestler, A.G. (Eds.), Hydrocarbon Seals: Importance for Exploration and Production. Norwegian Petroleum Society Special Publication, vol. 7, pp. 39- 50.
Lide, D.R. (Ed.), 1995. CRC Handbook of Chemistry and Physics. A Ready Reference Book of Chemical and Physical Data. CRC Press, Boca Raton, New York, London, Tokyo.
Lohrmann, J., Kukowski, N., Adam, J., Oncken, O., 2003. The impact of analogue material properties on the geometry, kinematics, and dynamics of convergent sand wedges. Journal of Structural Geology 25, 1691–1711.
Mandl, G., 2000. Faulting in Brittle Rocks. Springer, Berlin/Heidelberg/New York.
Margielewski, W., Urban, J., 2003. Crevice-type caves as initial forms of rock landslide development in the Flysch Carpathians. Geomorphology 54, 325–338.
Micarelli, L., Benedicto, A., Invernizzi, C., Saint-Bezar, B., Michelot, J.L., Vergely, P., 2005. Influence of *P*/*T* conditions on the style of normal fault initiation and growth in limestones from the SE-Basin, France. Journal of Structural Geology 27, 1577–1598.
Muir Wood, D., 1990. Soil Behaviour and Critical State Soil Mechanics. Cambridge University Press, New York.
Noweir, M.A., 2000. Back-thrust origin of the Hafit structure, northern Oman Mountain Front, United Arab Emirates. GeoArabia (Manama) 5, 215–228.
Otrtuno-Arzate, S., Ferket, H., Cacas, M.-C., Swennen, R., Roure, F., 2003. Late cretaceous carbonate reservoirs in the Cordoba platform and Veracruz Basin, Eastern Mexico. In: Bartolini, C., Buffler, R.T., Blickwede, J. (Eds.), The Circum-Gulf of Mexico and the Caribbean: Hydrocarbon Habitats, Basin Formation, and Plate Tectonics. AAPG Memoir 79, pp. 476–514.
Panien, M., 2004. Analogue Modelling Experiments of Basin Inversion Using Well-characterized Granular Materials and Comparison with Numerical Models. Ph.D. thesis. University of Bern.
Parry, R.H.G., 1995. Mohr Circles, Stress Paths and Geotechnics. E & FN Spon, London.
Patton, T.L., Fletcher, R.C., 1995. Mathematical block-motion model for deformation of a layer above a buried fault of arbitrary dip and sense of slip. Journal of Structural Geology 17, 1455–1472.
Peacock, D.C.P., Sanderson, D.J., 1995. Pull-aparts, shear fractures and pressure solution. Tectonophysics 241, 1–13.
Peacock, D.C.P., Zhang, X., 1993. Field examples and numerical modelling of oversteps and bends along normal faults in cross-section. Tectonophysics 234, 147–167.
Ramberg, H., 1981. Gravity, Deformation and the Earth's Crust, second ed. Academic Press, London and New York.
Ramsay, J.G., Huber, M.I., 1987. The Techniques of Modern Structural Geology. In: Folds and Fractures, vol. 2. Academic Press, London.
Roscoe, K.H., Schofield, A.N., 1963. Mechanical behaviour of an idealized 'wet' clay. In: Proceedings of the Second European Conference on SMFE. SMFE, Wiesbaden, pp. 47–54.
Sapra, A., 1997. Geological analysis of early water production in horizontal wells in the Middle EastAAPG International Conference and Exhibition, Vienna, Austria, Sept. 7–10, 1997. AAPG Bulletin 81, 1410.
Schmatz, J., 2006. Experimental Study on Clay Gouge Evolution in Mechanically Stratified Sequences. Dipl.-Geol. thesis. RWTH-Aachen University.
Schmatz, J., Holland, M., Giese, S., van der Zee, W., Urai, J.L. in press. Clay smear processes in mechanically layered sequences – results of water-saturated model experiments with free top surface. In: Mamtani, M. (Ed.), Structural Geology – from Classical to Modern Concepts. Journal of the Geological Society of India. Special Publication, Springer.
Schellart, W.P., 2000. Shear test results for cohesion and friction coefficients for different granular materials: scaling implications for their usage in analogue modelling. Tectonophysics 324, 1–16.
Schöpfer, M.P.J., Childs, C., Walsh, J.J., 2007a. Two-dimensional distinct element modelling of the structure and growth of normal faults in multilayer sequences: part 2. Impact of confining pressure and strength contrast on fault zone geometry and growth. Journal of Geophysical Research 112, B10404.
Schöpfer, M.P.J., Childs, C., Walsh, J.J., 2007b. Two-dimensional distinct element modelling of the structure and growth of normal faults in multilayer sequences. Part 1: model calibration, boundary conditions and selected results. Journal of Geophysical Research 112, B10401.
Schöpfer, M.P.J., Childs, C., Walsh, J.J., Manzocchi, T., Koyi, H., 2007c. Geometrical analysis of the refraction and segmentation of normal faults in periodically layered sequences. Journal of Structural Geology 29, 318–335.
Schreurs, G., Buiter, S.J.H., Boutelier, D., Corti, G., Costa, E., Cruden, A., Daniel, J.-M., Hoth, S., Koyi, H., Kukowski, N., Lohrmann, J., Ravaglia, A., Schlische, R.W., Withjack, M.O., Yamada, Y., Cavozzi, C., Delventisette, C., Brady, J.A.E., Hoffmann-Rothe, A., Mengus, J.-M., Montanari, D., Nilforoushan, F., 2006. Analogue benchmarks of shortening and extension experiments. In: Buiter, S.J.H., Schreurs, G. (Eds.), Analogue and Numerical Modelling of Crustal-Scale Processes. Geological Society, London, Special Publications, vol. 253, pp. 29–64.
Schweiger, A., Zimmermann, I., 1999. A new approach for the measurement of the tensile strength of powders. Powder Technology 101, 7–15.
Sibson, R.H., 1996. Structural permeability of fluid-driven fault-fracture meshes. Journal of Structural Geology 18, 1031–1042.
Sibson, R.H., 2000. Fluid involvement in normal faulting. Journal of Geodynamics 29, 469–499.
Sibson, R.H., 2003. Brittle-failure controls on maximum sustainable overpressure in different tectonic regimes. AAPG Bulletin 87, 901–908.
Sims, D.W., Morris, A.P., Ferrill, D.A., Wyrick, D.Y., Colton, S.L., 2003. Physical models of pit chain formation over dilatational faults in Mars. Lunar and Planetary Science XXXIV.
Tondi, E., 2007. Nucleation, development and petrophysical properties of faults in carbonate grainstones: evidence from the San Vito Lo Capo peninsula (Sicily, Italy). Journal of Structural Geology 29, 614–628.
Turcotte, D.L., Schubert, G., 2002. Geodynamics, second ed. Cambridge University Press, Cambridge, 456 pp.
Van der Zee, W., 2001. Dynamics of Fault Gouge Development in Layers Sand–Clay Sequences. Ph.D. thesis. RWTH Aachen University, Shaker Verlag, Aachen, Germany.
Van der Zee, W., Urai, J., Richard, P.D., 2003. Lateral clay injection into normal faults. GeoArabia 8, 501–522.
Van der Zee, W., Urai, J., 2005. Processes of normal fault evolution in a siliciclastic sequence: a case study from Miri, Sarawak, Malaysia. Journal of Structural Geology 27, 2281–2300.
Van Konijnenburg, J.-H., Massaferro, J.L., Mauduit, T., Richard, P., Willemse, M., Droste, H., Fenton, M., 2000. Explaining early water breakthrough in a tough carbonate reservoir: the Natih E formation, Al Ghubar Field, Oman. In: AAPG Annual Meeting, April 16–19, New Orleans, Louisiana.

Wallace, W., 1861. The Laws Which Regulate the Deposition of Lead Ores in Veins: Illustrated by an Examination of the Geological Structure of the Mining Districts of Alston Moor. Stanford, London.
Willemse, E.J.M., Peacock, D.C.P., Aydin, A., 1997. Nucleation and growth of strike-slip faults in limestones from Somerset, U.K. Journal of Structural Geology 19, 1461–1477.
Wolf, H., König, D., Triantafyllidis, T., 2003. Experimental investigation of shear band patterns in granular material. Journal of Structural Geology 25, 1229–1240.
Xiao, S., 1993. Gebirgsmechanische Untersuchungen zu Bruchmechanismen und zur Gebirgsdruckverteilung an Abbaurändern im Steinkohlengebirge. Ph.D. thesis. Technischen Universität Clausthal, Clausthal, Germany.